Trends and variability in the Southern Annular Mode over the Common Era

Jonathan King (jonking93@email.arizona.edu)
University of Arizona
Kevin Anchukaitis
The University of Arizona
Kathryn Allen
University of Tasmania
Tessa Vance
University of Tasmania
Amy Hessl
West Virginia University https://orcid.org/0000-0002-2279-6260

Article

Keywords:

Posted Date: August 17th, 2022

DOI: https://doi.org/10.21203/rs.3.rs-1958191/v1

Trends and variability in the Southern Annular Mode over the Common Era

Jonathan King[1,2*], Kevin J. Anchukaitis[1,2,3], Kathryn Allen[4,5,6], Tessa Vance[7] and Amy Hessl[8]

[1]Department of Geosciences, University of Arizona, Tucson, AZ 85721 USA.
[2]Laboratory of Tree-Ring Research, University of Arizona,Tucson, AZ 85721 USA.
[3]School of Geography, Development, and Environment,University of Arizona, Tucson, AZ 85721 USA.
[4]School of Geography, Planning and Spatial Sciences,University of Tasmania, Hobart 7001.
[5]School of Ecosystem and Forest Sciences,University of Melbourne, Richmond, VIC Australia 3121.
[6]Centre of Excellence for Australian Biodiversity and Heritage, University of New South Wales, Australia.
[7]Australian Antarctic Program Partnership,Institute for Marine and Antarctic Studies, University of Tasmania, Hobart, Australia.
[8]Department of Geology and Geography, West Virginia University, Morgantown, WV USA.

Abstract

The Southern Annular Mode (SAM) is the leading mode of atmospheric variability in the extratropical Southern Hemisphere and has wide ranging effects on ecosystems and societies. Despite the SAM's importance, paleoclimate reconstructions disagree on its variability and trends. Here, we use data assimilation to reconstruct the SAM over the last 2000 years using temperature and drought-sensitive climate proxies. Our method does not assume a stationary relationship between proxy records and the SAM over an instrumental calibration period, so our reconstruction is less sensitive to the teleconnection variability that has hindered previous reconstructions. Our approach also allows us to identify critical paleoclimate records and quantify reconstruction

uncertainty through time. We find no evidence for a forced response in SAM variability prior to the 20th century. We also find the modern positive trend is outside the range of the prior 2000 years, but only on multidecadal time scales.

Introduction

The Southern Annular Mode (SAM) is the leading mode of atmospheric variability in the extratropical Southern Hemisphere and is characterized by a mostly zonally-symmetric mass oscillation with anti-correlated pressure anomalies over the mid-latitudes and Antarctica [1–4, and see Figure 1]. The SAM's phases capture the strength and position of the mid-latitude westerly winds and the subtropical jet, such that positive phases promote a poleward shift of storm tracks and intensification of the circumpolar westerly belt, while negative phases promote an equator-ward shift of storm tracks and weakening of the westerly winds. Variability in the SAM therefore has wide ranging effects across the Southern Hemisphere. Positive phases of the SAM are linked to cooling over Australia and central Antarctica, as well as warming over the Antarctic Peninsula and southern South America [5–11]. Hydroclimate effects of the positive phase include drying over southern South America, western South Africa, southern Australia, and New Zealand, as well as increased precipitation over central and eastern Australia and southeastern South America [7, 10, 12–16]. SAM variations have also been linked to wildfire activity in South America and south-east Australia [17–21], changes in sea ice distribution [8, 22–25], and ocean-atmosphere carbon exchange [26–28]. Understanding SAM variability is therefore important for both societies and ecosystems throughout the Southern Hemisphere, particularly in sub-tropical-temperate regions projected to experience a future drying climate.

Since the 1950s, the SAM has exhibited a trend toward a more positive state [4, 29, 30], which is attributed to stratospheric ozone depletion and rising concentrations of atmospheric CO_2 [31–35]. This positive trend has potentially contributed to severe droughts, including the Day Zero Cape Town drought [36] and Millennium Drought in Australia [37, 38], as well as increased fire activity [17–19]. Given these impacts, it is important to place the SAM's recent behavior in a long-term perspective and assess the relative influence of anthropogenic forcing and natural climate variability. In the context of multi-decadal trends, reconstructions spanning multiple centuries are necessary to resolve forced responses from the SAM's internal variability. Instrumental records of the SAM only extend through the mid-1900s and longer reanalysis-derived indices show low correlations with one another and differences in variability prior to the 1950s [30, 39], so characterizing the SAM's long-term behavior requires paleoclimate reconstructions derived from natural climate archives.

There are several existing multi-century SAM reconstructions [40, 41, 42] (henceforth, V12, A14, and D18), but they show limited agreement prior to the 1850s [42, 43]. Most indicate a negative phase in the SAM during the late 1400s, but both trends and decadal-scale variability show large discrepancies aside from this feature.

There are several potential reasons for these differences. Firstly, all three reconstructions rely on the calibration of proxy records directly with an instrumental SAM index. This implicitly makes two important assumptions for each reconstruction: first, that the relationship of proxy records to local climate variables is stationary over time; and second, that the SAM's teleconnections with local climate variables are stationary and well-represented by the instrumental record. While the first is reasonable and a necessary assumption of most paleoclimate analyses, multiple studies cast doubt on this second point, and regional complexity in the climate response to specific SAM phases further decreases the likelihood of this assumption holding. For instance, even over the instrumental period, SAM exhibits non-stationary connections with precipitation and temperature anomalies in southern South America, Australasia, and the Antarctic Peninsula [13, 44], and many of the proxy records in existing SAM reconstructions come from these areas [43]. Evolving concentrations of greenhouse gases, stratospheric ozone, connections with ENSO, and stochastic climate variability can also affect the SAM's influence on regional climates over multi-decadal time scales [29, 32, 45, 46]. Pseudo-proxy experiments have also shown that non-stationary teleconnections cause reconstruction skill to vary widely with the selection of different calibration windows [47]. This effect is particularly pronounced for proxy networks with fewer than 20 sites, which is common in the early portions of SAM reconstructions. To mitigate such effects, D18 explicitly screened for stationarity in their reconstruction, although this required calibration with a longer and therefore less reliable observational record [48].

Differences between SAM reconstructions may also result from the selection of different reconstruction targets and proxy networks. For example, A14 targets an annual SAM index, whereas V12 and D18 target an austral summer (DJF) SAM index. D18 found that annual reconstructions were much more sensitive to the selection of proxy sites and calibration windows and they conclude that annual products may exhibit increased sensitivity to non-stationary teleconnections, which may partly explain the differences between the reconstructions. Additionally, each index has been reconstructed using a different proxy network with a different geographic extent. A14 targets the Drake Passage sector, using a mix of terrestrial proxy types from southern South America as well as Antarctic ice cores. In comparison, V12 targets the Pacific sector, using a network of tree-ring chronologies from South America and New Zealand. D18 uses the most spatially extensive network, including tree-ring records [40], Antarctic ice cores, PAGES2k South American proxies [49], and coral records from the tropical Pacific [50]. Furthermore, A14 utilizes a temperature-sensitive proxy network, while V12 and D18 leverage both temperature and hydroclimate-sensitive proxies. Given the variability of the SAM's teleconnections on regional scales [13, 44], and the climate sensitivities of different proxy types [48], these variations in proxy-network design may further help explain reconstruction differences. It is often difficult to assess the influence and contribution of individual proxy records in multiproxy reconstructions, so the cause of any reconstructed index's behavior are often unclear. This is particularly relevant in the period prior to 1400 CE, when the sparsity of proxy networks leaves the reconstructions vulnerable to the dominant influence of just a few records. Ultimately, as a consequence

of these uncertainties and the differences in existing reconstructions, the evolution of the SAM over the Common Era and its response to external forcing remains poorly constrained [43, 51].

To address these uncertainties, here we reconstruct the austral summer (DJF) SAM index over the Common Era at annual resolution using offline paleoclimate data assimilation (DA). DA is a recently developed reconstruction technique that integrates climate proxy records with the dynamical behavior captured by climate models [52, 53]. In brief, DA uses forward or proxy-system models [54, 55] to translate climate model states into the same dimensions or 'space' as a collection of climate proxy records. This allows direct comparison of the model output with the proxy records. The climate model states are then updated to more closely match the proxy records, and a model-derived estimate of climate system covariance is used to propagate the update to reconstruction targets, such as the SAM. DA has recently been used to reconstruct surface air temperature anomalies [56–59], geopotential height fields [57], the response to volcanic eruptions [60, 61], sea ice extent [62], sea surface temperatures [63], and hydroclimate variables [64]. In this study, we assimilate the PAGES2k temperature-sensitive proxy network [49], the South American Drought Atlas [SADA; 65], and the Australia-New Zealand Drought Atlas [ANZDA; 66] (Figure 1) using a suite of last millennium general-circulation climate models (see Methods and Supplemental Table 1) to reconstruct the austral summer SAM index over the last 2,000 years. Here, we follow Gong et al. [2] and define the SAM index using the difference of zonal-mean pressure anomalies (see Methods, Equation 1).

In the context of SAM reconstructions, DA offers several additional advantages relative to traditional methods. Firstly, our method does not calibrate proxy records against an instrumental SAM index directly; instead, we calibrate proxy forward models using local climate variables, like temperature and precipitation, near the proxy sites. Consequently, our calibration does not assume stationary SAM teleconnections and only requires the stability of proxy relationships to their local climate. Additionally, we estimate covariance between proxies and the SAM using thousands of years of climate model output. As a result of this, our proxy-SAM relationships are not sensitive to potentially anomalous decadal- or centennial-scale variations in the SAM's behavior. Furthermore, DA is amenable to the use of a range of proxy types as well as gridded climate records with spatial autocorrelation, and we leverage this to incorporate the two existing tree-ring based drought atlases into our reconstruction. Previous work indicates that SAM reconstructions using hydroclimate-sensitive sites are more skillful than those using strictly temperature-sensitive proxy networks [47]. Each drought atlas provides extensive coverage for at least the last five centuries and each incorporates over 150 tree-ring records. They therefore represent a significant source of hydroclimate information available for our reconstruction.

Finally, our DA method allows us to incorporate an optimal sensor analysis [67] as part of the final reconstruction. Traditionally, optimal sensor analyses have been used to identify ideal regions for future proxy development [67–70]; however, they can also be applied within a DA framework to quantitatively assess the power of different proxy sites as the overall network evolves through time. We use this to identify the proxy sites that are most likely to drive the reconstruction in each time

step, which helps characterize the reconstruction's overall behavior. This information is particularly useful in the early part of this Common Era reconstruction, when the sparse network size can give high weights to a limited number of records.

Results

We assess the skill of our SAM reconstruction relative to the Marshall [4] and Fogt indices [71, 72], two commonly used instrumental SAM indices (see Methods for further details). Before comparing time series, we first normalize the Fogt index and our reconstruction to the Marshall index, such that the mean and variance of the detrended normalized time series match those of the detrended Marshall index over the period 1958-2000 CE. This places all series in the same unit space while preserving differences in the instrumental trend. Examining skill values (Table 1; Figure 2, upper panel), we find that the reconstruction's correlation with the Marshall index (1958-2000 CE) is $r = 0.72 (p \ll 0.001)$, which is comparable to that reported for A14 ($r = 0.75, p \ll 0.001$)). With respect to the 20th century Fogt index, our reconstruction correlates at $r = 0.65, p \ll 0.001$), somewhat higher than A14 ($r = 0.51, p \ll 0.001$)). Our RMSE values with the Marshall index (1.45) are similar to, albeit slightly higher than, those reported by D18 (1.32). We emphasize that our reconstruction is not calibrated directly to the SAM index, so the agreement with the Marshall and Fogt indices is not built-in to our reconstruction method and thus represents a more independent skill metric.

We next characterize the reconstruction's behavior over the last two millennia (Figure 2, center). The reconstruction exhibits minimal evidence for trends over most of the first millennium of the Common Era, although the third and seventh centuries are both marked by increased multidecadal variability as the SAM alternates between negative and positive phases. A more strongly negative anomaly in the early 1000s is followed by a notable 100-year positive trend that concludes with the most positive anomalies outside of the instrumental era. The SAM persists in a positive state until the late 1400s, when it abruptly decreases to strongly negative values. After this event, the index returns to near-zero mean anomalies. It has a peak in the mid-1700s and begins exhibiting a positive trend in the early 1800s. This trend intensifies in the later half of the 20th century, and the reconstruction ends with the most positive SAM anomalies observed during the Common Era.

Reconstruction uncertainty ranges from ± 4.5 anomaly units in the early reconstruction to less than 2.3 after 1500 CE (Figure 2b). We note that, because we use a stationary prior, the reconstruction years are treated as fully independent of one another. While this is common in many reconstruction techniques, it does not represent the reality of the SAM, which exhibits persistence on interannual time scales due to potential connections with the stratosphere [73, 74], tropical variability [75, 76], and external forcing [35, 77]. One consequence of this is that the uncertainty estimates shown here likely overestimate the true reconstruction uncertainty. Overall, uncertainty decreases as the reconstruction approaches the present day, a result of the increasing size of the proxy network (Figure 2, bottom panel).

We use our optimal sensor framework to identify which proxies are most responsible for reducing reconstruction uncertainty over time (Figure 3). A proxy's ability to reduce uncertainty corresponds to its influence on the reconstruction, so this analysis also allows us to identify which proxies most strongly influence the reconstruction at a given point in time. The first 900 years of the reconstruction are most strongly affected by the Mt. Read (Tasmania) tree-ring record with additional support from the Plateau Remote, WDC06A, and WDC05A ice cores. At 900 CE, the Oroko (New Zealand) tree ring chronology joins the network and supplants Mt. Read as the most influential record. Two large decreases in reconstruction uncertainty occur in 1400 and 1500 CE, which correspond to the addition of the SADA and ANZDA, respectively.

Examining the reconstruction's response to external forcing, we find no coherence with the solar forcing series and no significant common response to major volcanic eruptions (Figure 4). By contrast, the reconstruction exhibits significant positive trends in the latter half of the twentieth century. However, these modern trends are only significant on time-scales greater than approximately 40 years; trends over shorter time scales fall within the reconstructed range of trends from natural variability. Here, we define natural variability using the distribution of trends in periods of the pre-industrial reconstruction. Examining the Marshall Index, we similarly find that trends shorter than about 35 years are within the reconstructed range of natural variability, but that trends longer than about 35 years fall outside this range. The Marshall Index exhibits its most positive, significant trends for intervals centered on the early 1980s. Although this period is near the end of our reconstruction and less well resolved than preceding decades, we note that the reconstruction similarly exhibits strongly-positive, significant trends centered on the early 1980s. Here we have quantified natural variability using the distribution of reconstructed trends over the period 1500-1900 CE, the years including both drought atlases. If we instead use the period of the full reconstruction (1-1900 CE), the tests become more stringent. Significant trend in the reconstruction is limited to the last 55-80 year interval, and Marshall Index trends are only significant when containing the interval 1964-2000 CE. We also experiment with using the early portion of the reconstruction (1-899 CE) to quantify natural variability and find these results are similar to those using the full reconstruction period (Supplemental Figure 1).

Discussion

Our reconstruction suggests that the SAM is dominated by internal variability at least throughout the pre-industrial Common Era. This finding is in agreement with D18, who likewise found minimal influence of solar and volcanic forcing on their reconstruction. Volcanic signals have likewise been a challenge to detect in Southern Hemisphere temperature reconstructions [78]. Some studies have proposed that that an observed relationship between SAM and ENSO [41, 76, 79–81] could provide a pathway for solar forcing [82] to influence the SAM [43, 83]; however, our results do not support this mechanism during the the Common Era. In a set of model simulations, Wright et al. [83] found that increasing the amplitude of the prescribed

solar variability lead to a significant relationship between solar forcing and the simulated SAM. These authors suggest that using high amplitude solar forcing could help reconcile SAM reconstructions with climate simulations; however, the lack of solar signals in our reconstruction differs notably from their findings and instead further supports the realism of low-amplitude solar forcing scenarios [84–86].

By contrast with solar and volcanic forcings, our analysis indicates that the most recent multi-decadal trend is outside the range of natural variability and reflects the SAM's response to anthropogenic forcing. We emphasize that this modern trend is only significant for intervals longer than about 40 years when assessed against the 1500-1900 CE period, or intervals of about 55 years when considering the full Common Era. Shorter trend periods remain within the range of natural variability, even for the most recent intervals. The significance of the modern positive trend therefore reflects its anomalous persistence, rather than the amplitude of its decadal-scale variation alone. The significance of these longer trends emphasizes the importance of the paleoclimate record, particularly given the uncertainties in instrumental SAM records prior to the late twentieth century [39, 87]. We also note that the modern positive trend is only outside of the range of natural variability for trends spanning the years from about 1940-2000 CE. Trends are generally not significant during the early 1900s, and are even negative for the 50 year period centered on the 1930s. These results help establish the onset of the modern positive trend at around 1940 CE. This timing coincides with increasing emissions of ozone-depleting substances and greenhouse gasses, and is consistent with literature attributing the modern trend to stratospheric ozone depletion and rising levels of atmospheric CO_2 [31–35].

We next compare our reconstruction with the V12, A14, and D18 products (Figure 5). We normalize the mean and variance of each index over the period 1400-1850 CE to allow comparison of the series in the same unit space. We select the year 1400 CE because it is the first year with values for all four reconstructions and we end the normalization in 1850 CE to limit the sensitivity of our comparison to differing representations of the post-industrial trend. All four indices agree on the existence of a strong positive trend during the late twentieth century; however, all show limited coherence with one another prior to about 1850 CE, as noted in previous studies [42, 43]. The limited agreement of these reconstructions reduces confidence in the significance of modern trends [51], and the causes of these discrepancies include differing seasonal expressions, different proxy networks, and the relative weights of proxies within those networks. Additionally, V12, A14, and D18 all rely on calibration with the instrumental SAM index, which can cause uncertainty when there is non-stationarity in the teleconnection of local climate with the SAM. Ultimately, our reconstruction does not solve the problem of differing reconstructions and similarly shows limited agreement with all of V12, A14, and D18. However, our assimilation does not rely on calibration with the SAM index, and offers a potential improvement by reducing uncertainty from non-stationary teleconnections.

An additional advantage of our reconstruction is the transparency provided by the optimal sensor's assessment of the relative weights and influence of proxy records in our network. In general, we find that our reconstruction is most strongly influenced by the two drought atlases, followed by the Mt. Read (Tasmania), Oroko (New

Zealand), and Pink Pine (New Zealand) tree ring chronologies, and also the Plateau Remote, Siple Station, WDC06A, and WDC06B ice cores. We note here that a minor change in reconstruction uncertainty does not imply that a proxy has a weak effect on the reconstruction, because highly influential proxies from the same location may present redundant climate signals. For example, the Pink Pine chronology is the third most potentially influential PAGES2k record (Figure 3, lower right), but has a relatively small effect on reconstruction uncertainty when added to the network in 1457 CE (Figure 3, center). This is because much of the Pink Pine climate signal is already represented by the nearby Oroko site. However, such redundant sites are valuable because they make the reconstruction less sensitive to non-climatic noise from a single highly-influential proxy record. In the case of Pink Pine and Oroko, spreading the southern New Zealand climate signal over two influential records allows either site to partially correct for non-climatic noise in the other. A proxy's potential influence reflects both its covariance with the SAM and the ability of our proxy estimates to accurately estimate the record. Ultimately, assuming our estimates of climate covariance are accurate, the influential sites are those most likely to contribute skill to the reconstruction.

Overall, we find that tree-ring chronologies from Tasmania and New Zealand, the West Antarctic ice cores, and the drought atlas locations in Tasmania, southern New Zealand, the eastern edge of Australia, and southeast South America all have the greatest potential for reconstructing SAM (Figure 3, upper panels). This suggests that additional proxy development in these regions, or extensions of shorter existing records such as the Oroko and Pink Pine tree-ring chronologies or the Siple Station ice core, would be valuable for improving the skill of future SAM reconstructions. However, we caution that location alone is not sufficient for proxy utility and that future proxy development must demonstrate a robust sensitivity to local climate that connects them to the SAM. We also note that, in our optimal sensor framework, a proxy's potential influence is a function of (1) the accuracy of our forward (proxy system) models, and (2) the covariance of the resulting proxy estimates with the SAM in the climate models. As a result, our analysis may currently undervalue proxies from regions with limited climate model agreement, and future improvements in both climate and proxy system models may allow paleoclimate data from other regions to contribute to skillful reconstructions of the SAM.

Conclusions

Our study provides the first reconstruction of the Southern Annular Mode at annual resolution over the entire Common Era. We use a data assimilation method that does not calibrate the proxies directly against the instrumental SAM index, so the reconstruction is not sensitive to observed SAM non-stationarity in the modern era. Our reconstruction leverages both the SADA and ANZDA in addition to the PAGES2k proxy network and represents a significant increase in paleoclimate information available to reconstruct the SAM. Optimal sensor analysis indicates that the first 1400 years of the reconstruction are strongly influenced by the Oroko and Mt. Read tree-ring chronologies, with additional support from the Plateau Remote, WDC06A, and

WDC05A ice cores. As the SADA and ANZDA are added to the proxy network (1400 CE and 1500 CE, respectively), the drought atlases become strong drivers of the reconstruction's behavior.

Our reconstruction provides a foundation with which to assess the drivers of the SAM's behavior over the Common Era; such assessments are critical given the SAM's importance to societies and effects on climate variability throughout the Southern Hemisphere. Although our index and existing SAM reconstructions show limited agreement with one another, all products exhibit the most strongly positive and persistent SAM trend during the last several decades. We find that the modern positive trend in the SAM is outside the range of natural variability over the previous millennium, further confirming a response to anthropogenic forcing. Prior to the most recent decades, we find no relationship between SAM variability and external climate forcing, suggesting that its behavior is dominated by internal variability over the pre-industrial Common Era.

Methods and Materials

Southern Annular Mode Index

In this study, we use the Gong et al. [2] definition of the SAM index:

$$\mathrm{SAM} = P^*_{40°\mathrm{S}} - P^*_{65°\mathrm{S}} \quad (1)$$

where P^*_X indicates the normalized zonal-mean sea level pressure (SLP) at a particular latitude. The latitudes 40°S and 65°S were selected as the zonal-means with the most strongly anti-correlated SLP anomalies across the mid- and high-latitude Southern Hemisphere. We use this definition, as opposed to an index derived from a principal component analysis because the latitudes of the most strongly anti-correlated SLP anomalies are robust across the climate models considered in our assimilation (Supplemental Tables 1, 2). We target the austral summer (DJF; December - February) SAM because this corresponds to the seasonality of the climate response of the majority of our proxy network. D18 also suggests that summer SAM reconstructions are more robust to proxy network design than annual reconstructions, which further supports this choice. When calculating the SAM index, we normalize seasonal mean values, rather than individual months. Austral summers span months from two calendar years, and this can introduce date ambiguities for annual records, particularly tree-ring chronologies. Throughout this paper, we use the convention that the year of an austral summer value matches the calendar year of the associated January.

Data Products

Reanalysis and Instrumental Indices

We use monthly precipitation and air-temperature fields from the Twentieth Century Reanalysis V3 [20CR; 88, 89] to calibrate our DA method. The 20CR is based on an 80-member ensemble Kalman Filter, and extends from 1850 CE to present at 2 degree resolution. Because of its role in our assimilation method, this effectively sets an upper bound on the resolution of any gridded spatial product used in this reconstruction. We also use the austral summer Marshall Index[4] and Fogt Index [71, 72] to assess the skill of our reconstruction in the modern era. The Marshall Index estimates the Gong et al. [2] definition of the SAM (Equation 1), and is based on data from 12 weather stations (6 near 40°S, and 6 near 65°S). Because it uses station data, the Marshall index is not subject to the spurious trends observed in high-latitude Southern Hemisphere reanalysis pressure fields [4]. The Fogt index is constructed using a principal component regression of station pressure data and calibrated to the Marshall index. These indices are commonly used as a comparison point for SAM reconstructions[40–42],

Climate Proxies

In this reconstruction, we assimilate the PAGES2k temperature-sensitive proxy network [49], the South American Drought Atlas (SADA) [65], and the Australia-New

Zealand Drought Atlas (ANZDA) [66]. We limit all three datasets to those sites or locations south of 25°S. Pseudo-proxy tests of other latitude bounds suggests that reconstruction skill is minimally affected by the use of more northward proxy sites and agreement with the instrumental record exhibits a slight maximum for a bound at 25°S (Supplemental Figure 2). Overall, this domain maximizes the number of SAM-sensitive proxy sites in our network, while minimizing the effects of distal proxies that primarily reflect other climate signals.

From the PAGES2k dataset, we include all sites from the PAGES2k global temperature reconstruction that have annual or sub-annual temporal resolution. To maintain a common timescale, we bin all sub-annual sites to annual resolution. Our PAGES2k network therefore consists of 40 proxy records: 12 tree-ring chronologies, 3 lake sediment cores, 5 corals, 19 ice-cores, and 1 borehole-derived temperature reconstruction (Supplemental Table 3). The tree-ring records are from Tasmania, New Zealand, and the central Andes. The longest two chronologies are from Mt. Read, Tasmania and Oroko, New Zealand, which begin in 494 BCE and 900 CE, respectively; the remaining tree chronologies mostly begin between 1450 CE and 1550 CE. The three lake sediment proxies are derived from the central and southern Andes. The longest record (Laguna Chepical) spans the complete Common Era, while Lagunas Escondida and Aculeo begin in 400 CE and 816 CE, respectively. The five coral records are from the Houtman Abrolhos Islands off the west coast of Australia and begin between 1795 CE and 1900 CE. The Antarctica ice core records have varying temporal coverage. Four sites cover the full Common Era (Plateau Remote, WDC06A, James Ross Island, WAIS-Divide), six more extend at least one millennium, and the remaining nine begin between 1140 CE and 1703 CE. The borehole reconstruction is from WAIS-Divide and begins in 8 CE. For the 40 proxy set, full coverage extends from 1903 CE to 1983 CE with 20 sites remaining by 2000 CE.

The SADA and ANZDA are gridded tree-ring reconstructions of the self-calibrated Palmer Drought Severity Index (PDSI) during austral summer at annual resolution [65, 66]. The SADA is derived from 286 temperature and precipitation-sensitive tree-ring chronologies and begins in 1400 CE. The atlas covers all of South America south of 12.25°S at 0.5°resolution. Similarly, ANZDA is derived from 176 tree-ring chronologies, as well as one coral record, and begins in 1500 CE. The ANZDA covers Australia east of 136.25°E, and New Zealand, also at 0.5°resolution. The SAM is strongly associated with droughts and pluvials in the domains of both atlases [65], supporting their inclusion in our network. Both atlases have significantly higher spatial resolution than the reanalysis data and climate model output used for our reconstruction method. To permit calculations that require the same spatial resolution, we bin both atlases to the lowest resolution spatial grid relevant to a given experiment. For the main reconstruction, after applying latitude screening, our SADA and ANZDA networks consist of 104 and 71 binned records, each on a 2° x 2.5°grid. It is worth noting that several of the PAGES2k tree ring records used in our reconstruction were also used to construct the drought atlases, and these repeat records might initially appear to duplicate information in the reconstruction. However, our Kalman filter method explicitly accounts for covariance between proxy records, and

down-weights proxies with repeated information accordingly. Additional details for this process can be found in the following section.

Reconstruction Method

Kalman Filter

Our reconstruction uses an ensemble Kalman Filter approach [EnKF; 90], which follows the update equation:

$$\mathbf{X_a} = \mathbf{X_p} - \mathbf{K}(\mathbf{Y} - \hat{\mathbf{Y}}) \tag{2}$$

in each reconstructed time step. Here, the $\mathbf{X_p}$ and $\mathbf{X_a}$ matrices are the initial (prior) and updated (analysis) ensembles of climate model states. Each row holds a target climate variable, and each column a different selection of climate model output (ensemble member). $\mathbf{Y}$ is a matrix of proxy values for the time step; the columns of $\mathbf{Y}$ are constant, and each row holds the value from a particular proxy record repeated once for each ensemble member. $\hat{\mathbf{Y}}$ holds the model estimates of the proxy values; each row has the estimates for a particular proxy site, and each column has the estimates from a particular ensemble member. $\mathbf{K}$ is the Kalman gain:

$$\mathbf{K} = \mathrm{cov}(\mathbf{X_p}, \hat{\mathbf{Y}})[\mathrm{cov}(\hat{\mathbf{Y}}) + \mathbf{R}]^{-1} \tag{3}$$

where $\mathbf{R}$ is the matrix of proxy error-covariances. As previously mentioned, the Kalman filter accounts for duplication of information across repeated proxy records. This occurs via the $\mathrm{cov}(\hat{\mathbf{Y}})$ term in Equation 3, which reduces proxy weights in the Kalman gain as a function of shared proxy covariance. Note that any shared covariance derived from proxies' relationships with the SAM is balanced by the $\mathrm{cov}(\mathbf{X_p}, \hat{\mathbf{Y}})$ term in Equation 3. We use a square-root variant of EnKF [91, 92]. This modifies equations 2 and 3 to update the ensemble mean and deviations separately, and precludes the need for perturbed observations [93]. The Kalman filter can be expressed as a recursive Bayesian filter [94, 95], so we will often refer to $\mathbf{X_p}$ and $\mathbf{X_a}$ as the prior and posterior in this paper.

Prior

We construct the prior using output from climate models with paleoclimate simulations of the last millennium (Supplemental Table 1). We use a multi-model ensemble (MME), which has been found to reduce error relative to single model assimilations [59, 96]. Our MME consists of CCSM4, CESM-LME, MPI, and MRI, which represent the set of last millennium simulations with spatial resolutions greater than or at the resolution of the 20CR reanalysis. As such, this selection does not require us to bin the drought atlases to lower resolutions than 20CR, which allows us to extract maximum information from SADA and ANZDA. We also tested a larger MME consisting of 10 models with last millennium simulations regardless of resolution. Our tests show that the high-resolution MME maximizes reconstruction skill (Supplemental Figure 3). For CCSM4, MPI, and MRI, we use output from the

PMIP3 last1000 (850-1850 CE) and historical (1851-2005 CE) experiments, specifically ensemble member r1i1p1. For CESM-LME, we use output from full-forcing run 2 (850-2005 CE). While the PAGES2k proxy network does include stable oxygen isotope proxies, there are too few high-resolution last millennium isotope-enabled paleoclimate model simulations available to construct a multi-model prior[96].

We use an offline, stationary prior for our assimilation. Offline approaches [97, 98] differ from classical Kalman Filters in that updates are not used to inform model simulation. Instead, offline methods use pre-existing model output to build the prior in each time step. The offline approach has been shown to compare favorably with classical (online) methods in paleoclimate contexts but at a fraction of the computational cost [99, 100]. The stationary prior indicates that we use the same ensemble as the prior for each reconstructed time step. This is common in paleoclimate DA applications [52, 57, 101] and is justified by the limited forecast skill of climate models beyond the annual reconstruction time scale [102]. However, stationary priors have been observed to artificially reduce the variability of reconstructions as proxy networks become more sparse [59]. Consequently, our use of stationary priors necessitates a correction for the reconstruction's variability, which is detailed in the methods below.

To build each prior, we first calculate the DJF SAM time-series for each model, normalizing zonal SLP means to the pre-industrial period (850-1849 CE). We then concatenate the SAM index time-series from each model in every year of model output. The final prior has a total of 4624 ensemble members from 4 high-resolution models.

Proxy Forward Models and Error Covariances

The proxy modeling process begins by designing a forward model for each assimilated proxy record. For the PAGES2k records, we follow previous studies [53, 59] and use simple univariate linear models:

$$\hat{\mathbf{Y}} = a\mathbf{T} + b \tag{4}$$

where $\hat{\mathbf{Y}}$ is a vector of proxy estimates, and T is a vector of seasonal temperature means. Here, the seasonal means used for each site is taken from the seasonal sensitivity reported in the PAGES2k metadata [49]. We determine the coefficients a and b by calibrating each proxy PAGES2k record to the corresponding climate data from 20CR. For each proxy site, we first determine the seasonal sensitivity and then linearly regress the proxy record against the seasonal-mean temperature vector from the closest 20CR grid point in all overlapping years from 1950 - 2000 CE. The regression slope and intercept are then used as coefficients a and b. For the drought atlases, we estimate proxies by calculating PDSI [103] using the Thornthwaite estimation of potential evapotranspiration [104]. This uses monthly mean temperature and precipitation from a drought atlas grid cell to compute monthly PDSI values for each year. We then use the austral summer means of these monthly values as the proxy estimates. Effectively:

$$\mathbf{Y} = \text{mean}[\ \text{PDSI}_{\text{Thornthwaite}}(\mathbf{T}, \mathbf{P})\ ]_{\text{DJF}} \tag{5}$$

where T and P are monthly temperature and precipitation, and Y is the drought atlas estimate. We estimate proxy values for the model priors by applying Equations 4 and 5 to climate model output and matching each year's estimates to the associated ensemble member in the prior.

Although the PDSI calculation in Equation 5 uses the Thornthwaite approximation, both drought atlases target an observational dataset based on the Penman-Monteith method [65, 66, 105]. However, both the Thornthwaite and Penman-Monteith equations have been shown to perform similarly when applied to pre-industrial simulations, and this agreement occurs because the simplifying assumptions of the Thornthwaite method remain valid over the relatively confined range of last millennium temperatures [106]. For the purposes of this study, the Thornthwaite method provides two further advantages: First, the Thornthwaite equation is more computationally tractable, which allows us to apply it to the large spatial regions and the multiple millennium-length climate model simulations used for priors in our assimilation method. Second, because the Thornthwaite calculation requires fewer climate model data fields to estimate the PDSI [104, 105], opportunities for climate model biases to degrade the reconstruction are reduced.

We next estimate the proxy error covariances. These error covariances describe the uncertainty in the comparison of observed records to the proxy estimates $(\mathbf{Y} - \mathbf{Ye})$. In a classical Kalman Filter, the estimates $(\hat{\mathbf{Y}})$ are known perfectly and this uncertainty is derived from the observations $(\mathbf{Y})$, so $\mathbf{R}$ is often referred to as observation uncertainty. In paleoclimate contexts, this situation is inverted: proxy measurements are typically precise and uncertainty derives from the simplifications and parameterizations inherent in the estimation equations. Hence, we quantify R by running Equations 4 and 5 on the 20CR dataset (from 1950-2000 CE) and comparing the estimated proxy values to the real records. The differences between the two sets of values are used to estimate the errors inherent in using simple models and relatively coarse climate data to estimate the temporal behavior of the proxy records. Most EnKF paleoclimate efforts assume that proxy errors are independent, such that $\mathbf{R}$ is a diagonal matrix [52, 53, 57, 64]. This is justified for datasets like PAGES2k, for which proxy uncertainties are dominated by local biological, physical, and mechanistic effects [48]. However, the drought atlas grid points are strongly spatially correlated, so this assumption is not appropriate in this study. Instead, we calculate independent error-variances for the proxies in the PAGES2k network, and full error-covariances for both SADA and ANZDA. Hence, $\mathbf{R}$ is block-diagonal, rather than strictly diagonal. We estimate uncertainty in the final reconstruction from the spread of the assimilation posterior.

Variance Correction

The use of stationary priors creates artifacts in the variability of raw reconstruction. As the proxy network becomes sparse, less information is incorporated in the Kalman Filter, and the updated state is less able to move off the prior mean. This causes reconstruction variability to increase with the size of the proxy network and independently of the climatological record. We apply a variance adjustment scheme

to correct for this effect. Variance adjustments are common in paleoclimate reconstructions [107–110] and are inherent to simpler methods like Composite Plus Scale [111].

Here, we use a series of frozen-network assimilations to adjust temporal variance. There are five sites in our proxy network with observations in every year of the reconstruction. We first assimilate this five-site network over the full interval 1-2000 CE to derive a baseline time-series that is not affected by changes to the proxy network. We next determine each unique set of proxy sites used to update one or more time steps in the reconstruction. We then assimilate each set of proxies over the time steps for which all of the proxies have recorded values, and determine the ratio of this assimilation's standard deviation to that of the baseline time series over all overlapping years:

$$P(\text{set}) = \sigma_{\text{set}}/\sigma_{\text{Baseline}} \tag{6}$$

We then calculate a scaling factor for each time step using the normalized ratio for the associated proxy set:

$$w(t) = P(\text{set}(t))/\max(P) \tag{7}$$

A comparison of the raw and variance-adjusted reconstructions is provided in Supplemental Figure 4.

Optimal Sensor Analysis

We follow a previously established framework for optimal sensor analyses [67]. In brief, the method quantifies the ability of proxy sites to reduce the variance of a metric in a posterior ensemble. Here, we use the SAM as our metric, so the optimal sensor analysis here assesses the ability of sites to reduce uncertainty in the index across the reconstruction posterior. We first compute the total reduction in SAM posterior variance using the complete set of proxies with observations in each time step. We also quantify each site's ability to reduce reconstruction uncertainty when no other sites are in the proxy network. We refer to this quantity as 'potential percent constrained variance'.

External Forcing Analyses

We begin our external forcing analysis by investigating the SAM's response to natural climate forcings. We first use a wavelet coherence analysis to examine the relationship between our SAM reconstruction and a time series of reconstructed solar forcing [110, 112]. We next use a superposed epoch analysis [113] to determine the reconstruction's composite mean response to major volcanic eruptions. We used the eVolv2k V3 volcanic forcing dataset [114, 115] to select events with a total forcing magnitude greater than or equal to that of Krakatoa. This yielded 28 eruption years: 87, 169, 266, 433, 536, 540, 574, 626, 682, 817, 939, 1108, 1171, 1182, 1230, 1257, 1276, 1286, 1345, 1458, 1600, 1640, 1695, 1783, 1809, 1815, 1831, and 1883. For the SEA, we normalized each event to the mean of the preceding 5 years and examined the composite mean response over the 10 years following volcanic events. We tested

the significance of the observed response by bootstrapping 5,000 SEA time series via random draws of 28 event years from the remaining years in the reconstruction.

We next consider the SAM's response to anthropogenic forcings using both our reconstruction and the Marshall index. Before quantifying trends, we first normalize our reconstruction to the Marshall index, such that the mean and variance of the detrended normalized reconstruction matches those of the detrended Marshall index over the years of common overlap (1958-2000 CE). This places the series in the same unit space while preserving differences in the instrumental trend. We then calculate moving trends for the reconstruction over the years 1900-2000 CE using trend window lengths from 31 to 101 years. Similarly, we calculate moving trends for the Marshall Index over the years 1958-2020 CE using trend window lengths from 31 to 63 years. We then use the reconstruction to assess the significance of these trends. For each trend window length, we calculate the distribution of trends with the given window length from the reconstruction over the years 1500-1900 CE, and we define this distribution as the natural variability for that trend length. We then use the 90% confidence intervals of each distribution to determine a significance threshold for trends of the associated length. We also repeat this process using trend distributions from the intervals 1-1900 CE and 1-899 CE to examine the sensitivity of this analysis to different portions of the reconstruction.

Caveats and Limitations

Our DA method does not require a calibration with the instrumental SAM, which limits its sensitivity to non-stationarity in the SAM during the instrumental era. However, the trade-off is the influence of proxy forward model and climate model biases on the reconstruction. In the case of proxy models, any biases typically reduce the weight of the proxy in the assimilation, thereby limiting its effect on the reconstruction. We note that improving the accuracy or sophistication of the proxy forward models could increase the influence of many records; for example, transitioning the statistical forward models used here for the PAGES2k sites to more mechanistically accurate proxy system models [54] could potentially improve the reconstruction [101]. However, efforts to develop more complex proxy system models must also exercise caution, as excessive complexity and poorly constrained parameters may lead to overfitting and artificially high skill in the instrumental era at the expense of accuracy during the earlier reconstruction. In this study, we retain the simpler statistical forward models because (1) the PAGES2k proxies are reported to be temperature sensitive [49], (2) statistical proxy models remain the most common and tractable approach for paleoclimate data assimilation to date [53, 57, 59], and (3) the simple statistical model eliminates errors caused by the interaction of climate model biases with forward models that rely on absolute units.

With respect to climate models, biases in the mean state can affect proxy estimates that include parametrizations or thresholds based on absolute units. However, covariance biases are a greater concern, as they introduce errors in the propagation of information from the proxy records to the reconstruction target. For example, some of the climate models considered in this study simulate a SAM pattern that is too zonally symmetric and that overestimates the SAM's influence on overall Southern

Hemisphere circulation [116]. Such teleconnection biases can cause the assimilation to overestimate the covariance between various proxies and the SAM, thereby increasing reconstruction error. In this study, we use a multi-model ensemble (MME) to reduce the effects of covariance bias from any one model [59, 96]. We note that we weight each model equally, which effectively treats each model as independent. In reality, many models share common features or code, so this equal weighting may bias an ensemble towards the most similar models [117, 118]. For example, the CCSM4 and CESM-LME output used in our MME are both from models developed by the US National Center for Atmospheric Research (NCAR) and may more closely resemble one another than the MPI or MRI models. Future efforts may wish to test different model composition and weights when constructing a MME prior.

Finally, our use of a stationary offline prior implies a stationary estimate of climate system covariance when considered over the full reconstruction period. Although we use a long-term estimate of the SAM's climate covariance, the true covariance may vary on multi-decadal scales [13, 44], and these variations will not be captured in our approach. While the assumption of a reasonably stationary covariance is implicitly common to most spatial reconstruction methods [119, 120], the application of transient offline priors [102, 121, 122] or online assimilation techniques [123] may enhance future data assimilation reconstruction, although these approaches must balance the utility of evolving covariance estimates with reduced ensemble sizes.

Acknowledgments

We thank David Meko for providing the original PDSI estimation code on which ours is based. This research is supported by a grant from the US National Science Foundation's Paleo Perspectives on Climatic Change program (P2C2) AGS-1803946 to K.J.A. and A.H. T.V. is supported by an Australian Research Council Special Research Initiative for Antarctic Gateway Partnership (SR140300001) and the Australian Antarctic Program Partnership (ASCI000002). K.A. is supported by a grant from the Australian Research Council (FT200100102). We acknowledge the World Climate Research Programme's Working Group on Coupled Modelling, which is responsible for CMIP, and we thank the climate modeling groups for producing and making available their model output.

Author contributions

K.J.A., A.H., and J.K. designed the research. J.K. wrote all the software and code, improved and enhanced the assimilation method, conducted all calculations, and produced all the figures. A.H., T.V., and K.A. provided guidance, data, and knowledge for individual proxies and Southern Hemisphere climate variability. All authors (J.K., K.J.A., A.H., T.V. and K.A.) interpreted results and wrote the paper.

Competing interests

The authors declare that they have no conflicts of interest.

Data and code availability

The data and code used to produce this analysis, as well as the final reconstruction, will be made publicly available in a Zenodo repository with a permanent DOI pending review.

Supplementary materials

Supplemental Figure 1: Trend analysis using the early reconstruction (1-899 CE) to quantify natural variability and trend significance.

Supplemental Figure 2: Correlation of reconstructions with the Marshall Index as a function of latitude cutoff thresholds.

Supplemental Figure 3: Comparison of reconstruction skill using different multi-model priors.

Supplemental Figure 4: Raw and variance-adjusted reconstruction time series.

Supplemental Table 1: Climate models tested in assimilation priors.

Supplemental Table 2: Latitudes of maximum negative SLP correlation in climate models and 20CR.

Supplemental Table 3: PAGES2k sites used in the final reconstruction.

References

[1] Rogers, J. C. & Van Loon, H. Spatial variability of sea level pressure and 500 mb height anomalies over the southern hemisphere. *Monthly Weather Review* **110** (10), 1375–1392 (1982) .

[2] Gong, D. & Wang, S. Definition of antarctic oscillation index. *Geophysical Research Letters* **26** (4), 459–462 (1999) .

[3] Thompson, D. W. & Wallace, J. M. Annular modes in the extratropical circulation. part i: Month-to-month variability. *Journal of Climate* **13** (5), 1000–1016 (2000) .

[4] Marshall, G. J. Trends in the southern annular mode from observations and reanalyses. *Journal of Climate* **16** (24), 4134–4143 (2003) .

[5] Thompson, D. W. & Solomon, S. Interpretation of recent southern hemisphere climate change. *Science* **296** (5569), 895–899 (2002) .

[6] Kwok, R. & Comiso, J. C. Spatial patterns of variability in antarctic surface temperature: Connections to the southern hemisphere annular mode and the southern oscillation. *Geophysical Research Letters* **29** (14), 50–1 (2002) .

[7] Gillett, N. P., Kell, T. D. & Jones, P. Regional climate impacts of the southern annular mode. *Geophysical Research Letters* **33** (23) (2006) .

[8] Gupta, A. S. & England, M. H. Coupled ocean–atmosphere–ice response to variations in the southern annular mode. *Journal of Climate* **19** (18), 4457–4486 (2006) .

[9] Marshall, G. J., Orr, A., Van Lipzig, N. P. & King, J. C. The impact of a changing southern hemisphere annular mode on antarctic peninsula summer temperatures. *Journal of Climate* **19** (20), 5388–5404 (2006) .

[10] Hendon, H. H., Thompson, D. W. & Wheeler, M. C. Australian rainfall and surface temperature variations associated with the southern hemisphere annular mode. *Journal of Climate* **20** (11), 2452–2467 (2007) .

[11] Van Lipzig, N. P., Marshall, G. J., Orr, A. & King, J. C. The relationship between the southern hemisphere annular mode and antarctic peninsula summer temperatures: Analysis of a high-resolution model climatology. *Journal of Climate* **21** (8), 1649–1668 (2008) .

[12] Silvestri, G. E. & Vera, C. S. Antarctic oscillation signal on precipitation anomalies over southeastern south america. *Geophysical Research Letters* **30** (21) (2003) .

[13] Silvestri, G. & Vera, C. Nonstationary impacts of the southern annular mode on southern hemisphere climate. *Journal of Climate* **22** (22), 6142–6148 (2009) .

[14] Cai, W. & Cowan, T. Sam and regional rainfall in ipcc ar4 models: Can anthropogenic forcing account for southwest western australian winter rainfall reduction? *Geophysical Research Letters* **33** (24) (2006) .

[15] Reason, C. & Rouault, M. Links between the antarctic oscillation and winter rainfall over western south africa. *Geophysical Research Letters* **32** (7) (2005) .

[16] Kidston, J., Renwick, J. & McGregor, J. Hemispheric-scale seasonality of the southern annular mode and impacts on the climate of new zealand. *Journal of Climate* **22** (18), 4759–4770 (2009) .

[17] Holz, A. & Veblen, T. T. Variability in the southern annular mode determines wildfire activity in patagonia. *Geophysical Research Letters* **38** (14) (2011) .

[18] Mariani, M. & Fletcher, M.-S. The southern annular mode determines interannual and centennial-scale fire activity in temperate southwest tasmania, australia. *Geophysical Research Letters* **43** (4), 1702–1709 (2016) .

[19] Holz, A. *et al.* Southern annular mode drives multicentury wildfire activity in southern south america. *Proceedings of the National Academy of Sciences* **114** (36), 9552–9557 (2017) .

[20] Abram, N. J. *et al.* Connections of climate change and variability to large and extreme forest fires in southeast australia. *Communications Earth & Environment* **2** (1), 1–17 (2021) .

[21] Lim, E.-P. *et al.* The 2019 southern hemisphere stratospheric polar vortex weakening and its impacts. *Bulletin of the American Meteorological Society* **102** (6), E1150–E1171 (2021) .

[22] Hall, A. & Visbeck, M. Synchronous variability in the southern hemisphere atmosphere, sea ice, and ocean resulting from the annular mode. *Journal of Climate* **15** (21), 3043–3057 (2002) .

[23] Stammerjohn, S. E., Martinson, D., Smith, R., Yuan, X. & Rind, D. Trends in antarctic annual sea ice retreat and advance and their relation to el niño–southern oscillation and southern annular mode variability. *Journal of Geophysical Research: Oceans* **113** (C3) (2008) .

[24] Simpkins, G. R., Ciasto, L. M., Thompson, D. W. & England, M. H. Seasonal relationships between large-scale climate variability and antarctic sea ice concentration. *Journal of Climate* **25** (16), 5451–5469 (2012) .

[25] Kohyama, T. & Hartmann, D. L. Antarctic sea ice response to weather and climate modes of variability. *Journal of Climate* **29** (2), 721–741 (2016) .

[26] Lovenduski, N. S., Gruber, N., Doney, S. C. & Lima, I. D. Enhanced co2 outgassing in the southern ocean from a positive phase of the southern annular mode. *Global Biogeochemical Cycles* **21** (2) (2007) .

[27] Lovenduski, N. S., Fay, A. R. & McKinley, G. A. Observing multidecadal trends in southern ocean co2 uptake: What can we learn from an ocean model? *Global Biogeochemical Cycles* **29** (4), 416–426 (2015) .

[28] Sallée, J.-B., Speer, K. & Rintoul, S. Zonally asymmetric response of the southern ocean mixed-layer depth to the southern annular mode. *Nature Geoscience* **3** (4), 273–279 (2010) .

[29] Thompson, D. W., Wallace, J. M. & Hegerl, G. C. Annular modes in the extratropical circulation. part ii: Trends. *Journal of Climate* **13** (5), 1018–1036 (2000) .

[30] Fogt, R. L. & Marshall, G. J. The southern annular mode: variability, trends, and climate impacts across the southern hemisphere. *Wiley Interdisciplinary Reviews: Climate Change* **11** (4), e652 (2020) .

[31] Arblaster, J. M. & Meehl, G. A. Contributions of external forcings to southern annular mode trends. *Journal of Climate* **19** (12), 2896–2905 (2006) .

[32] Thompson, D. W. *et al.* Signatures of the antarctic ozone hole in southern hemisphere surface climate change. *Nature Geoscience* **4** (11), 741–749 (2011) .

[33] Polvani, L. M., Waugh, D. W., Correa, G. J. & Son, S.-W. Stratospheric ozone depletion: The main driver of twentieth-century atmospheric circulation changes in the southern hemisphere. *Journal of Climate* **24** (3), 795–812 (2011) .

[34] England, M. R., Polvani, L. M., Smith, K. L., Landrum, L. & Holland, M. M. Robust response of the amundsen sea low to stratospheric ozone depletion. *Geophysical Research Letters* **43** (15), 8207–8213 (2016) .

[35] Jones, J. M. *et al.* Assessing recent trends in high-latitude southern hemisphere surface climate. *Nature Climate Change* **6** (10), 917–926 (2016) .

[36] Sousa, P. M., Blamey, R. C., Reason, C. J., Ramos, A. M. & Trigo, R. M. The 'day zero' cape town drought and the poleward migration of moisture corridors. *Environmental Research Letters* **13** (12), 124025 (2018) .

[37] Verdon-Kidd, D. C. & Kiem, A. S. Nature and causes of protracted droughts in southeast australia: Comparison between the federation, wwii, and big dry droughts. *Geophysical Research Letters* **36** (22) (2009) .

[38] Cai, W., Van Rensch, P., Borlace, S. & Cowan, T. Does the southern annular mode contribute to the persistence of the multidecade-long drought over southwest western australia? *Geophysical Research Letters* **38** (14) (2011) .

[39] Barrucand, M. G., Zitto, M. E., Piotrkowski, R., Canziani, P. & O'Neill, A. Historical sam index time series: linear and nonlinear analysis. *International Journal of Climatology* **38**, e1091–e1106 (2018) .

[40] Villalba, R. *et al.* Unusual southern hemisphere tree growth patterns induced by changes in the southern annular mode. *Nature Geoscience* **5** (11), 793–798 (2012) .

[41] Abram, N. J. *et al.* Evolution of the southern annular mode during the past millennium. *Nature Climate Change* **4** (7), 564–569 (2014) .

[42] Dätwyler, C. *et al.* Teleconnection stationarity, variability and trends of the southern annular mode (sam) during the last millennium. *Climate Dynamics* **51** (5), 2321–2339 (2018) .

[43] Hessl, A., Allen, K. J., Vance, T., Abram, N. J. & Saunders, K. M. Reconstructions of the southern annular mode (sam) during the last millennium. *Progress in Physical Geography* **41** (6), 834–849 (2017) .

[44] Gallant, A. J., Phipps, S. J., Karoly, D. J., Mullan, A. B. & Lorrey, A. M. Nonstationary australasian teleconnections and implications for paleoclimate reconstructions. *Journal of Climate* **26** (22), 8827–8849 (2013) .

[45] Brönnimann, S. *et al.* Tropical circulation and precipitation response to ozone depletion and recovery. *Environmental Research Letters* **12** (6), 064011 (2017) .

[46] Yun, K.-S. & Timmermann, A. Decadal monsoon-enso relationships reexamined. *Geophysical Research Letters* **45** (4), 2014–2021 (2018) .

[47] Huiskamp, W. & McGregor, S. Quantifying southern annular mode paleoreconstruction skill in a model framework. *Climate of the Past* **17** (5), 1819–1839 (2021) .

[48] Jones, P. D. *et al.* High-resolution palaeoclimatology of the last millennium: a review of current status and future prospects. *The Holocene* **19** (1), 3–49 (2009) .

[49] PAGES2k Consortium. A global multiproxy database for temperature reconstructions of the common era. *Scientific Data* **4** (2017) .

[50] Tierney, J. E. *et al.* Tropical sea surface temperatures for the past four centuries reconstructed from coral archives. *Paleoceanography* **30** (3), 226–252 (2015) .

[51] Gulev, S. K. *et al.* in *Changing State of the Climate System* (eds Masson-Delmotte, V. *et al.*) *Climate Change 2021: The Physical Science Basis. Contribution of Working Group I to the Sixth Assessment Report of the Intergovernmental Panel on Climate Change* Ch. 2 (Cambridge University Press, 2021).

[52] Steiger, N. J., Hakim, G. J., Steig, E. J., Battisti, D. S. & Roe, G. H. Assimilation of time-averaged pseudoproxies for climate reconstruction. *Journal of Climate* **27** (1), 426–441 (2014) .

[53] Hakim, G. J. *et al.* The last millennium climate reanalysis project: Framework and first results. *Journal of Geophysical Research: Atmospheres* **121** (12), 6745–6764 (2016) .

[54] Evans, M. N., Tolwinski-Ward, S. E., Thompson, D. M. & Anchukaitis, K. J. Applications of proxy system modeling in high resolution paleoclimatology. *Quaternary Science Reviews* **76**, 16–28 (2013) .

[55] Dee, S. *et al.* Prysm: An open-source framework for proxy system modeling, with applications to oxygen-isotope systems. *Journal of Advances in Modeling Earth Systems* **7** (3), 1220–1247 (2015) .

[56] Goosse, H. *et al.* The role of forcing and internal dynamics in explaining the "medieval climate anomaly". *Climate Dynamics* **39** (12), 2847–2866 (2012) .

[57] Tardif, R. *et al.* Last millennium reanalysis with an expanded proxy database and seasonal proxy modeling. *Climate of the Past* **15** (4), 1251–1273 (2019) .

[58] Neukom, R., Steiger, N., Gómez-Navarro, J. J., Wang, J. & Werner, J. P. No evidence for globally coherent warm and cold periods over the preindustrial common era. *Nature* **571** (7766), 550–554 (2019) .

[59] King, J. M. *et al.* A data assimilation approach to last millennium temperature field reconstruction using a limited high-sensitivity proxy network. *Journal of Climate* 1–64 (2021) .

[60] Zhu, F., Emile-Geay, J., Hakim, G. J., King, J. & Anchukaitis, K. J. Resolving the differences in the simulated and reconstructed temperature response to volcanism. *Geophysical Research Letters* **47** (8), e2019GL086908 (2020) .

[61] Zhu, F. *et al.* A re-appraisal of the ENSO response to volcanism with paleoclimate data assimilation. *Nature Communications* **13** (1) (2022). https://doi.org/10.1038/s41467-022-28210-1 .

[62] Dalaiden, Q., Goosse, H., Rezsöhazy, J. & Thomas, E. R. Reconstructing atmospheric circulation and sea-ice extent in the west antarctic over the past 200 years using data assimilation. *Climate Dynamics* 1–25 (2021) .

[63] Tierney, J. E. *et al.* Glacial cooling and climate sensitivity revisited. *Nature* **584** (7822), 569–573 (2020) .

[64] Steiger, N. J., Smerdon, J. E., Cook, E. R. & Cook, B. I. A reconstruction of global hydroclimate and dynamical variables over the common era. *Scientific Data* **5** (1), 1–15 (2018) .

[65] Morales, M. S. *et al.* Six hundred years of south american tree rings reveal an increase in severe hydroclimatic events since mid-20th century. *Proceedings of the National Academy of Sciences* **117** (29), 16816–16823 (2020) .

[66] Palmer, J. G. *et al.* Drought variability in the eastern australia and new zealand summer drought atlas (anzda, ce 1500–2012) modulated by the interdecadal pacific oscillation. *Environmental Research Letters* **10** (12), 124002 (2015) .

[67] Comboul, M., Emile-Geay, J., Hakim, G. J. & Evans, M. N. Paleoclimate sampling as a sensor placement problem. *Journal of Climate* **28** (19), 7717–7740 (2015) .

[68] Bradley, R. S. Jones, P. D., Bradley, R. S. & Jouzel, J. (eds) *Are there optimum sites for global paleotemperature reconstruction?* (eds Jones, P. D., Bradley, R. S. & Jouzel, J.) *Climatic Variations and Forcing Mechanisms of the Last 2000 Years*, 603–624 (Springer Berlin Heidelberg, Berlin, Heidelberg, 1996).

[69] Evans, M. N., Kaplan, A. & Cane, M. A. Optimal sites for coral-based reconstruction of global sea surface temperature. *Paleoceanography* **13** (5), 502–516 (1998) .

[70] Mauger, G., Bumbaco, K., Hakim, G. & Mote, P. Optimal design of a climatological network: Beyond practical considerations. *Geoscientific Instrumentation, Methods and Data Systems* **2** (2), 199–212 (2013) .

[71] Fogt, R. L. *et al.* Historical sam variability. part ii: Twentieth-century variability and trends from reconstructions, observations, and the ipcc ar4 models. *Journal of Climate* **22** (20), 5346–5365 (2009) .

[72] Jones, J. M. *et al.* Historical sam variability. part i: Century-length seasonal reconstructions. *Journal of Climate* **22** (20), 5319–5345 (2009) .

[73] Lim, E.-P., Hendon, H. & Thompson, D. Seasonal evolution of stratosphere-troposphere coupling in the southern hemisphere and implications for the predictability of surface climate. *Journal of Geophysical Research: Atmospheres* **123** (21), 12–002 (2018) .

[74] Byrne, N. J., Shepherd, T. G. & Polichtchouk, I. Subseasonal-to-seasonal predictability of the southern hemisphere eddy-driven jet during austral spring and early summer. *Journal of Geophysical Research: Atmospheres* **124** (13), 6841–6855 (2019) .

[75] L'Heureux, M. L. & Thompson, D. W. Observed relationships between the el niño–southern oscillation and the extratropical zonal-mean circulation. *Journal of Climate* **19** (2), 276–287 (2006) .

[76] Wilson, A. B., Bromwich, D. H. & Hines, K. M. Simulating the mutual forcing of anomalous high southern latitude atmospheric circulation by el niño flavors and the southern annular mode. *Journal of Climate* **29** (6), 2291–2309 (2016) .

[77] Gillett, N. P., Fyfe, J. C. & Parker, D. E. Attribution of observed sea level pressure trends to greenhouse gas, aerosol, and ozone changes. *Geophysical Research Letters* **40** (10), 2302–2306 (2013) .

[78] PAGES 2k-PMIP3 group. Continental-scale temperature variability in PMIP3 simulations and PAGES 2k regional temperature reconstructions over the past millennium. *Climate of the Past* **11** (12), 1673–1699 (2015). https://doi.org/10.5194/cp-11-1673-2015 .

[79] Ding, Q., Steig, E. J., Battisti, D. S. & Wallace, J. M. Influence of the tropics on the southern annular mode. *Journal of Climate* **25** (18), 6330–6348 (2012) .

[80] Fogt, R. L., Bromwich, D. H. & Hines, K. M. Understanding the sam influence on the south pacific enso teleconnection. *Climate Dynamics* **36** (7), 1555–1576 (2011) .

[81] Fogt, R. L. & Bromwich, D. H. Decadal variability of the enso teleconnection to the high-latitude south pacific governed by coupling with the southern annular mode. *Journal of Climate* **19** (6), 979–997 (2006) .

[82] Emile-Geay, J., Cobb, K. M., Mann, M. E. & Wittenberg, A. T. Estimating central equatorial pacific sst variability over the past millennium. part ii: Reconstructions and implications. *Journal of Climate* **26** (7), 2329–2352 (2013) .

[83] Wright, N. M., Krause, C. E., Phipps, S. J., Boschat, G. & Abram, N. J. Influence of long-term changes in solar irradiance forcing on the southern annular mode. *Climate of the Past* **18** (6), 1509–1528 (2022) .

[84] Ammann, C. M., Joos, F., Schimel, D. S., Otto-Bliesner, B. L. & Tomas, R. A. Solar influence on climate during the past millennium: Results from transient simulations with the NCAR Climate System Model. *Proceedings of the National Academy of Sciences* **104** (10), 3713–3718 (2007) .

[85] Hind, A. & Moberg, A. Past millennial solar forcing magnitude. *Climate dynamics* **41** (9), 2527–2537 (2013) .

[86] Schurer, A. P., Tett, S. F. & Hegerl, G. C. Small influence of solar variability on climate over the past millennium. *Nature Geoscience* **7** (2), 104–108 (2014) .

[87] Ho, M., Kiem, A. & Verdon-Kidd, D. The southern annular mode: a comparison of indices. *Hydrology and Earth System Sciences* **16** (3), 967–982 (2012) .

[88] Compo, G. P. *et al.* The twentieth century reanalysis project. *Quarterly Journal of the Royal Meteorological Society* **137** (654), 1–28 (2011) .

[89] Slivinski, L. C. *et al.* Towards a more reliable historical reanalysis: Improvements for version 3 of the twentieth century reanalysis system. *Quarterly Journal of the Royal Meteorological Society* **145** (724), 2876–2908 (2019) .

[90] Evensen, G. Sequential data assimilation with a nonlinear quasi-geostrophic model using monte carlo methods to forecast error statistics. *Journal of Geophysical Research: Oceans* **99** (C5), 10143–10162 (1994) .

[91] Andrews, A. A square root formulation of the kalman covariance equations. *AIAA Journal* **6** (6), 1165–1166 (1968) .

[92] Tippett, M. K., Anderson, J. L., Bishop, C. H., Hamill, T. M. & Whitaker, J. S. Ensemble square root filters. *Monthly Weather Review* **131** (7), 1485–1490 (2003) .

[93] Whitaker, J. S. & Hamill, T. M. Ensemble data assimilation without perturbed observations. *Monthly Weather Review* **130** (7), 1913–1924 (2002) .

[94] Chen, Z. *et al.* Bayesian filtering: From kalman filters to particle filters, and beyond. *Statistics* **182** (1), 1–69 (2003) .

[95] Wikle, C. K. & Berliner, L. M. A bayesian tutorial for data assimilation. *Physica D: Nonlinear Phenomena* **230** (1-2), 1–16 (2007) .

[96] Parsons, L. A. *et al.* Do multi-model ensembles improve reconstruction skill in paleoclimate data assimilation? *Earth and Space Science* **8** (4), e2020EA001467 (2021) .

[97] Oke, P. R., Allen, J. S., Miller, R. N., Egbert, G. D. & Kosro, P. M. Assimilation of surface velocity data into a primitive equation coastal ocean model.

Journal of Geophysical Research: Oceans **107** (C9), 5–1 (2002) .

[98] Evensen, G. The ensemble kalman filter: Theoretical formulation and practical implementation. *Ocean Dynamics* **53** (4), 343–367 (2003) .

[99] Matsikaris, A., Widmann, M. & Jungclaus, J. On-line and off-line data assimilation in palaeoclimatology: a case study. *Climate of the Past* **11** (1), 81–93 (2015) .

[100] Acevedo, W., Fallah, B., Reich, S. & Cubasch, U. Assimilation of pseudo-tree-ring-width observations into an atmospheric general circulation model. *Climate of the Past* **13** (5), 545–557 (2017) .

[101] Dee, S. G., Steiger, N. J., Emile-Geay, J. & Hakim, G. J. On the utility of proxy system models for estimating climate states over the common era. *Journal of Advances in Modeling Earth Systems* **8** (3), 1164–1179 (2016) .

[102] Bhend, J., Franke, J., Folini, D., Wild, M. & Brönnimann, S. An ensemble-based approach to climate reconstructions. *Climate of the Past* **8** (3), 963–976 (2012) .

[103] Palmer, W. C. *Meteorological drought* Vol. 30 (US Department of Commerce, Weather Bureau, 1965).

[104] Thornthwaite, C. W. An approach toward a rational classification of climate. *Geographical Review* **38** (1), 55–94 (1948) .

[105] Allen, R., Smith, M., Perrier, A. & Pereira, L. S. An update for the definition of reference evapotranspiration. *ICID bulletin* **43** (2), 1–34 (1994) .

[106] Smerdon, J. E., Cook, B. I., Cook, E. R. & Seager, R. Bridging past and future climate across paleoclimatic reconstructions, observations, and models: A hydroclimate case study. *Journal of Climate* **28** (8), 3212–3231 (2015) .

[107] Cook, E. R., Meko, D. M., Stahle, D. W. & Cleaveland, M. K. Drought reconstructions for the continental united states. *Journal of Climate* **12** (4), 1145–1162 (1999) .

[108] Esper, J., Frank, D. C., Wilson, R. J. & Briffa, K. R. Effect of scaling and regression on reconstructed temperature amplitude for the past millennium. *Geophysical Research Letters* **32** (7) (2005) .

[109] Frank, D., Esper, J. & Cook, E. R. Adjustment for proxy number and coherence in a large-scale temperature reconstruction. *Geophysical Research Letters* **34** (16) (2007) .

[110] Anchukaitis, K. J. *et al.* Last millennium northern hemisphere summer temperatures from tree rings: Part ii, spatially resolved reconstructions. *Quaternary*

Science Reviews **163**, 1–22 (2017) .

[111] Mann, M. E. & Jones, P. D. Global surface temperatures over the past two millennia. *Geophysical Research Letters* **30** (15) (2003) .

[112] Schmidt, G. *et al.* Climate forcing reconstructions for use in pmip simulations of the last millennium (v1.1). *Geoscientific Model Development* **5** (1), 185–191 (2012) .

[113] Haurwitz, M. W. & Brier, G. W. A critique of the superposed epoch analysis method: its application to solar–weather relations. *Monthly Weather Review* **109** (10), 2074–2079 (1981) .

[114] Sigl, M. *et al.* Timing and climate forcing of volcanic eruptions for the past 2,500 years. *Nature* **523** (7562), 543–549 (2015) .

[115] Toohey, M. & Sigl, M. Volcanic stratospheric sulfur injections and aerosol optical depth from 500 bce to 1900 ce. *Earth System Science Data* **9** (2), 809–831 (2017) .

[116] Zheng, F., Li, J., Clark, R. T. & Nnamchi, H. C. Simulation and projection of the southern hemisphere annular mode in cmip5 models. *Journal of Climate* **26** (24), 9860–9879 (2013) .

[117] Knutti, R., Masson, D. & Gettelman, A. Climate model genealogy: Generation cmip5 and how we got there. *Geophysical Research Letters* **40** (6), 1194–1199 (2013) .

[118] Sanderson, B. M., Knutti, R. & Caldwell, P. A representative democracy to reduce interdependency in a multimodel ensemble. *Journal of Climate* **28** (13), 5171–5194 (2015) .

[119] Tingley, M. P. *et al.* Piecing together the past: statistical insights into paleoclimatic reconstructions. *Quaternary Science Reviews* **35**, 1–22 (2012) .

[120] Amrhein, D. E., Hakim, G. J. & Parsons, L. A. Quantifying structural uncertainty in paleoclimate data assimilation with an application to the last millennium. *Geophysical Research Letters* **47** (22), e2020GL090485 (2020) .

[121] Franke, J., Valler, V., Brönnimann, S., Neukom, R. & Jaume-Santero, F. The importance of input data quality and quantity in climate field reconstructions–results from the assimilation of various tree-ring collections. *Climate of the Past* **16** (3), 1061–1074 (2020) .

[122] Osman, M. B. *et al.* Globally resolved surface temperatures singe the last glacial maximum. *Nature* **599**, 239–244 (2021) .

[123] Perkins, W. A. & Hakim, G. J. Reconstructing paleoclimate fields using online data assimilation with a linear inverse model. *Climate of the Past* **13** (5), 421–436 (2017) .

Metric	Marshall Index (1958-2000)	Fogt Index (1958-2000)	Fogt Index (1866-2000)
Correlation ($p \ll 0.001$)	0.72	0.67	0.56
RMSE	1.45	1.56	1.80
σ Ratio	0.97	1.03	1.15
Mean Bias	-0.26	0.45	-0.29

Table 1: Reconstruction Skill metrics for the Southern Annular Mode calculated against instrumental indices over the given time periods

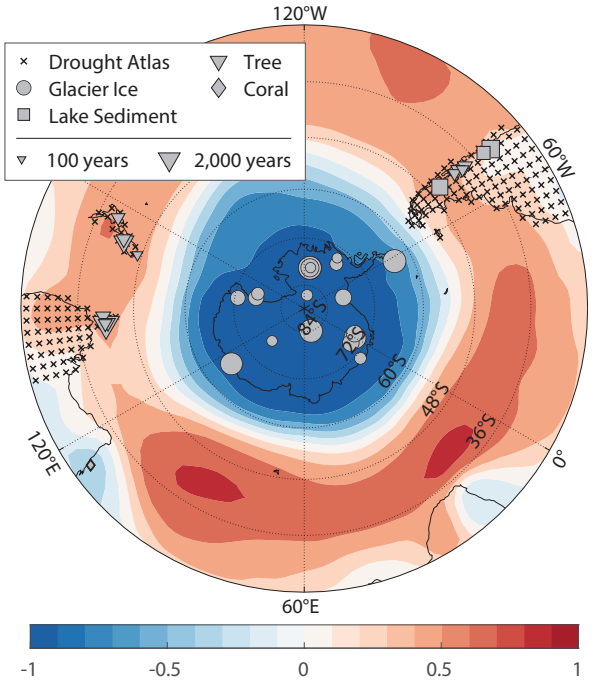

Fig. 1: Map of the proxy network. Black Xs indicate the centroid of binned drought atlas sites. Grey markers indicate PAGES2k sites. The size of the PAGES2k markers correspond to the length of each record. Filled color contours show the field correlation between the SAM index and DJF sea level pressure from 20CR [88, 89] over the period 1958-2000 CE.

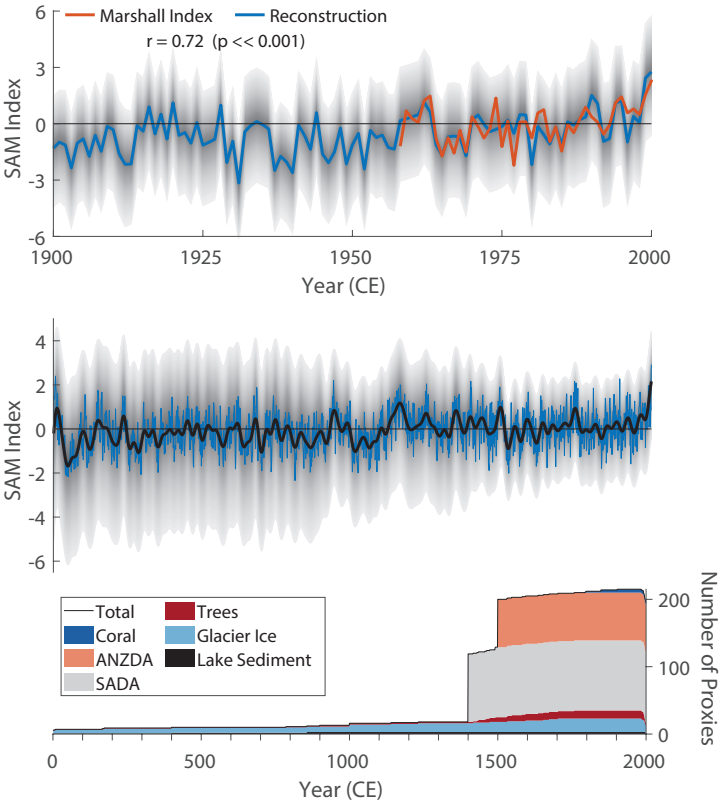

Fig. 2: Evolution of the reconstruction over time. Top: Comparison of the annual reconstruction (blue) with the Marshall index (red) over the instrumental era. Shading indicates the 5-95 percentiles of the reconstruction. Middle: Evolution of the annual reconstruction (blue) and 31-year lowpass filtered (black) over the Common Era. Shading indicates the 5-95 percentiles of the lowpass filtered series. Bottom: Composition of the proxy network over time. Colors for proxy types are as follows: Dark blue (coral), pink (ANZDA), grey (SADA), dark red (trees), light blue (glacier ice), black (lake sediment).

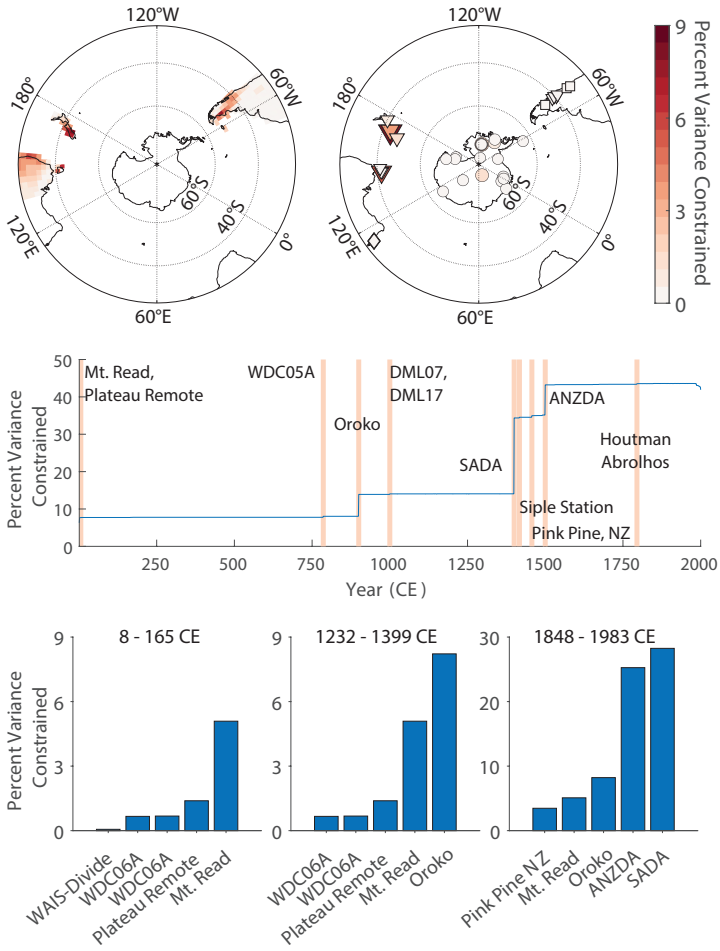

Fig. 3: Optimal Sensor Analysis. Top: Maps of the potential ability for drought atlas (left) and PAGES2k (right) sites to constrain reconstruction posterior variance. Middle: Evolution of reconstruction posterior variance over time. Yellow bars indicate the addition of the indicated proxy to the network. Bottom: Ranked histograms of the seven sites with greatest potential influence in the early reconstruction (left), immediately before the addition of drought atlases (middle) and for the full network (right). Potential influence is determined as the uncertainty constrained by a single-proxy network.

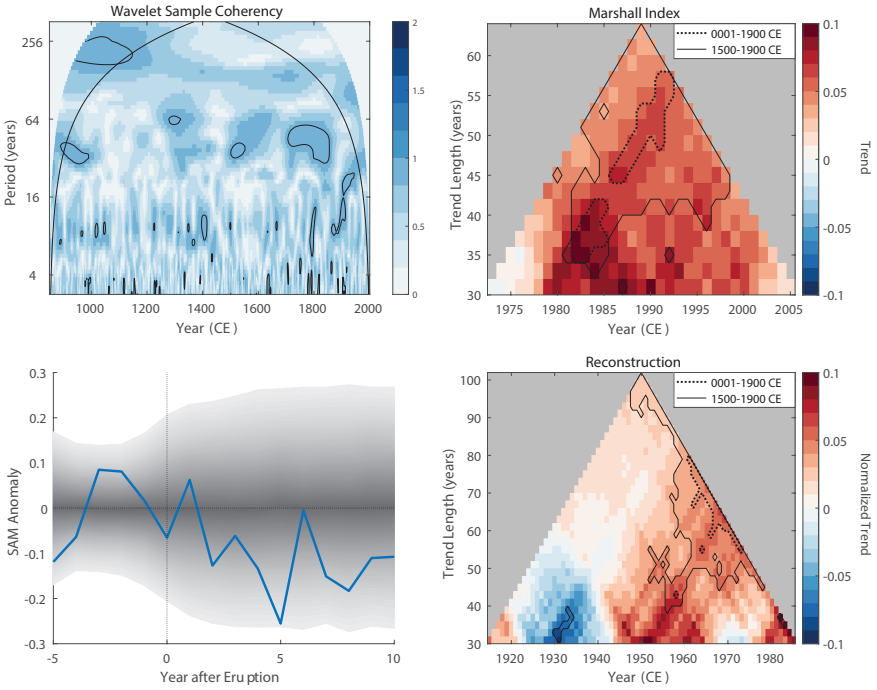

Fig. 4: SAM climate responses. Top left: Wavelet coherence of the reconstructed SAM index with the solar forcing reconstruction [112]. Bottom left: Composite mean response to major volcanic eruptions. Shading indicates 5-95 percentiles. Blue line is the ensemble mean. Right: Instrumental SAM trends for the Marshall Index (top right) and reconstruction (bottom right). Colored points indicate trends calculated from a sliding window centered on the given year. Solid (dotted) contours surround statistically significant trends at the 90% confidence interval relative to the reconstruction over the period 1500-1900 CE (1-1900 CE).

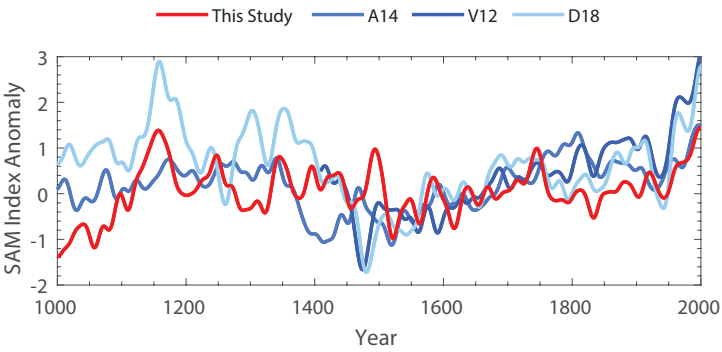

Fig. 5: Comparison of SAM reconstructions over the last millennium. All reconstructions are smoothed via a 30-year Gaussian filter and normalized to the period 1400-1850 CE.

Supplementary Files

This is a list of supplementary files associated with this preprint. Click to download.

- Supplement.pdf